Geophysical Research Letters

RESEARCH LETTER
10.1029/2020GL089557

An 18-Year Climatology of Directional Stratospheric Gravity Wave Momentum Flux From 3-D Satellite Observations

N. P. Hindley[1], C. J. Wright[1], L. Hoffmann[2], T. Moffat-Griffin[3], and N. J. Mitchell[1,3]

[1]Centre for Space, Atmospheric and Oceanic Science, University of Bath, Bath, UK, [2]Jülich Supercomputing Centre, Forschungszentrum Jülich, Jülich, Germany, [3]Atmosphere, Ice and Climate Group, British Antarctic Survey, Cambridge, UK

Key Points:
- Directional stratospheric gravity wave momentum flux (GWMF) is derived from global 3-D AIRS/Aqua satellite observations from 2002 to 2019
- Dramatic reductions and reversals of high-latitude GWMF are seen during SSWs; in the tropics the SAO modulates the AIRS GWMF but not the QBO
- A lateral convergence of wintertime GWMF toward 60°S occurs each year that has no counterpart in the Northern Hemisphere

Supporting Information:
- Supporting Information S1

Correspondence to:
N. P. Hindley,
n.hindley@bath.ac.uk

Citation:
Hindley, N. P., Wright, C. J., Hoffmann, L., Moffat-Griffin, T., & Mitchell, N. J. (2020). An 18-year climatology of directional stratospheric gravity wave momentum flux from 3-D satellite observations. *Geophysical Research Letters*, *47*, e2020GL089557. https://doi.org/10.1029/2020GL089557

Received 6 JUL 2020
Accepted 1 NOV 2020
Accepted article online 9 NOV 2020

Abstract Atmospheric gravity waves (GWs) are key drivers of the atmospheric circulation, but their representation in general circulation models (GCMs) is challenging, leading to significant biases in middle atmospheric circulations. Unresolved GW momentum transport in GCMs must be parameterized, but global directional GW observations are needed to constrain this. Here we present an 18-year climatology of directional stratospheric GW momentum flux (GWMF) from global AIRS/Aqua 3-D satellite observations during 2002 to 2019. Striking hemispheric asymmetries are found at high latitudes, including dramatic reductions and reversals of GWMF during sudden stratospheric warmings. During Southern Hemisphere winter, a lateral convergence of GWMF toward 60°S is found that has no Northern Hemisphere counterpart. In the tropics, we find that zonal GWMF in AIRS measurements is strongly modulated by the semiannual oscillation (SAO) but not the quasi-biennial oscillation (QBO). Our results provide guidance for future GW parameterizations needed to resolve long-standing biases in GCMs.

Plain Language Summary Gravity waves (GWs) are traveling waves that can occur in geophysical fluid environments subject to the gravitational force. In the Earth's atmosphere, GWs transport momentum that helps to drive the atmospheric circulation, especially in the middle atmosphere. But for numerical weather and climate models, accurately simulating GWs has proven very challenging because of a lack of GW observations, leading to significant model biases. Here we present an 18-year climatology of GW observations near 40-km altitude for 2002 to 2019. For the first time, we present multidecadal global measurements of directional GW momentum flux derived from 3-D satellite observations from National Aeronautics and Space Administration's (NASA's) AIRS instrument. We find that during Southern Hemisphere winter, GWs travel laterally toward 60°S each year. This is significant because most models underestimate GW momentum near 60°S and do not typically include lateral propagation in their parameterizations. In the tropical stratosphere, we find no modulation of GWs in AIRS observations by the quasi-biennial oscillation (QBO). This is consistent with the hypothesis that GW-QBO interactions occur at shorter vertical wavelengths, which are invisible to AIRS. Our results will help to guide future GW parameterizations, leading to more accurate atmospheric simulations and ultimately better forecasts of weather and climate.

1. Introduction

The accurate representation of atmospheric gravity waves (GWs) in general circulation models (GCMs) has been a major challenge for the atmospheric dynamics community in recent years (e.g., Alexander et al., 2010; Fritts & Alexander, 2003; Fritts et al., 2006; Geller et al., 2013; Plougonven et al., 2020). Since the first atmospheric models were created, realistic simulation of the middle atmosphere was not possible without the momentum driving of these mesoscale waves, forcing the atmospheric state away from radiative equilibrium. For most climate models and GCMs however, a large fraction of the GW spectrum is subgrid and must be parameterized (e.g., Alexander et al., 2010; Charron et al., 2002; Kim et al., 2003; Warner & McIntyre, 1996). Inaccurate representation of GWs in GCMs can result in large wind and temperature biases, such as the long-standing wintertime "cold-pole" problem at southern high latitudes (Butchart et al., 2011; Garfinkel & Oman, 2018; Garcia et al., 2017; McLandress et al., 2012). Even as the spatial resolution of modern GCMs is increased with improved computer power and more GWs are explicitly resolved,

models are still reliant on the parameterization of the salient effects of unresolved waves to produce realistic circulations (e.g., Kim et al., 2003; Vosper, 2015; Vosper et al., 2016). However, these parameterizations are poorly constrained in both magnitude and behavioral effects due to a lack of global measurements of GW properties (Alexander et al., 2010; Plougonven et al., 2020). Further, no single instrument can observe the full GW spectrum, an effect known as the observational filter (M. J. Alexander, 1998; Alexander & Barnet, 2007; Preusse et al., 2002).

A key quantity that must be constrained by observations is the vertical flux of horizontal pseudo-momentum due to GWs, also known simply as GW momentum flux (GWMF), which determines potential momentum forcing on the background winds via wave breaking and saturation processes. However, GWs are three-dimensional (3-D) phenomena. To fully constrain their directional GWMF, 3-D observations are needed. Three-dimensional stratospheric measurements are notoriously challenging and are normally limited to specialist instrumentation (Ern et al., 2004; Krisch et al., 2017, 2018, 2020). Combinations of instruments (e.g., Alexander, 2015; Faber et al., 2013; Wright et al., 2016), or the use of supplementary wind information (e.g., Alexander & Barnet, 2007; Alexander et al., 2009), have been used to infer 3-D GW structure, but these require limiting assumptions and are confined to colocated and/or coincident measurements.

As a result, global directional GWMF measurements have proven elusive. In recent years however, the development of a 3-D temperature retrieval for AIRS/Aqua by Hoffmann and Alexander (2009), combined with the development of 3-D spectral analysis techniques for GW measurements (Ern et al., 2017; Hindley et al., 2019; Lehmann et al., 2012; Wright et al., 2017), has allowed global 3-D GW measurements to be made. These 3-D measurements can provide directional GWMF climatologies, which can inform and constrain future parameterizations in GCMs. As discussed by Plougonven et al. (2020), it is not a straightforward process to simply take GW measurements and convert them directly into model parameterizations, but global directional GWMF measurements are an essential missing piece of the puzzle. For high-resolution GW-resolving models, the AIRS observational filter and sampling can even be applied to the model to compare resolved and measured GWMF directly (Hindley et al., 2020). Observations can also improve our understanding of key aspects of GW behavior such as intermittency (Hertzog et al., 2012; Jewtoukoff et al., 2015), lateral propagation (Hindley et al., 2015, 2019; Kalisch et al., 2014; Preusse et al., 2014), and secondary wave generation (Bacmeister & Schoeberl, 1989; Becker & Vadas, 2018; Bossert et al., 2017; Heale et al., 2020; Kogure et al., 2020; Satomura & Sato, 1999; Woods & Smith, 2010; Yasui et al., 2018) that can be used to guide future parameterizations.

Here we present an 18-year climatology of stratospheric GWMF derived from AIRS/Aqua observations for the period 2002–2019. For the first time, directional GWMF is computed globally over two decades using 3-D observations analysed with a specialized 3-D *S*-transform technique. To our knowledge, this is the largest observational study of atmospheric GWs performed so far. GWMF results shown here correspond to the AIRS observational window for GWs (vertical wavelengths $\lambda_z \gtrsim 15$ km and horizontal wavelengths $\lambda_H \lesssim 800$ km). In section 2 we describe the 3-D AIRS data set and our analysis method. In section 3 we present our GWMF results and we draw our conclusions in section 4.

2. Data and Methods

2.1. Three-Dimensional AIRS/Aqua Satellite Observations

Hoffmann and Alexander (2009) developed a high-resolution 3-D temperature retrieval for the AIRS instrument on National Aeronautics and Space Administration's (NASA's) Aqua satellite (Aumann et al., 2003; Chahine et al., 2006). Launched in 2002 in sun-synchronous polar orbit, Aqua passes over the same surface location twice each day. AIRS measures data in a continuous 1,780 km wide swath of 90 across-track elements, with 13.5 km (across-track) and 18 km (along-track) spacing at nadir (Hoffmann et al., 2014). The retrieval scheme of Hoffmann and Alexander (2009) uses infrared radiances in the 15 μm and 4.3 μm channels to derive a vertical temperature profile for each measurement footprint. This provides 3-D stratospheric temperature measurements between 10 and 70 km altitude, with 3 km vertical spacing for altitudes below 60 km. The retrieval is optimized for GW analysis. Retrieval noise and vertical resolution are balanced to give an effective vertical resolution varying between 7 km at 20 km altitude and 15 km at 60 km altitude (Ern et al., 2017; Hoffmann & Alexander, 2009; Meyer & Hoffmann, 2014; Sato et al., 2016). Noise is lowest between 20 and 60 km, at approximately 1.4 to 2 K (Ern et al., 2017; Hindley et al., 2019; Hoffmann &

Alexander, 2009). Sensitivity of the retrieval to GWs is discussed in Meyer and Hoffmann (2014), Hindley et al. (2019), and Ern et al. (2017).

GW temperature perturbations are extracted from large-scale "background" variations by subtracting a fourth-order polynomial fit from each cross-track row (Alexander & Barnet, 2007; Hoffmann et al., 2014; Hindley et al., 2016; Wu, 2004; Wright et al., 2017). This reduces sensitivity to cross-track horizontal wavelengths $\lambda_H \gtrsim 800$ km (Hoffmann et al., 2014, their Figure 5). A 3×3 horizontal boxcar filter is applied to each vertical layer to mitigate the effect of AIRS retrieval noise (Hindley et al., 2019; Wright et al., 2017), which reduces our sensitivity to waves with $\lambda_H \lesssim 50-75$ km. In the vertical, we interpolate onto a regular 1.5 km altitude grid. Measurements above 60 km and below 20 km are set to zero, with a smooth half-bell taper applied to reduce edge effects near the boundaries as described by Hindley et al. (2019). This limits our visibility to vertical wavelengths greater than around 40 km. An estimated sensitivity function for 3-D AIRS GW measurements near 40 km altitude for different horizontal and vertical wavelengths, after Ern et al. (2017) and Hindley et al. (2019), is provided in Figure S1 in the supporting information for the present paper.

2.2. Measuring 3-D GW Properties

To measure the spectral properties of GWs, we apply a 3-D *S*-transform (3DST) technique as described by Hindley et al. (2019). Based upon Stockwell et al. (1996), this provides estimates of the dominant wave amplitudes, wavelengths and directions at every location in a 3-D data volume. This method has been applied to 3-D AIRS data and other geophysical data sets in several recent studies (Hindley et al., 2016, 2019; Hu, Ma, Yan, Hindley, Xu, & Jiang, 2019; Hu, Ma, Yan, Hindley, & Zhao, 2019; Wright et al., 2017).

Our AIRS analysis here is identical to that used by Hindley et al. (2019). For each "granule" of AIRS measurements (135 along-track rows), the 3DST is computed for the 1,000 frequencies with the largest spectral amplitudes. This reduces required computational time by a factor of ~10 compared to analysing all available frequencies, with a negligible effect on the results (Hindley et al., 2019). This approach is ideal for long-timescale analyses here, giving us measurements of the dominant (largest spectral amplitude) spectral properties at each location along the AIRS scan-track between 20 to 60 km altitude.

Since AIRS measurements are instantaneous in time, we must break a directional ambiguity in our 3-D measurements. Previous studies have assumed GW propagation directions to be opposite to the prevailing wind (e.g., Alexander et al., 2009). Here, however, we assume that measured waves are upwardly propagating (vertical wavenumber $m < 0$), which constrains the horizontal direction (Ern et al., 2017; Hindley et al., 2019; Wright et al., 2017). This approach is preferential here because the horizontal directionality arises freely from our observations, rather than being forced by supplementary wind information from reanalyses, which can exhibit significant biases at AIRS altitudes (Wright & Hindley, 2018). As discussed later in section 3.2, in practice we find that when upward propagation is assumed, large-scale GW propagation in the stratosphere is almost always opposite to the background winds at mid to high latitudes, so it is likely that both assumptions are appropriate for AIRS observations.

We apply our analysis globally for the period September 2002 to September 2019, analysing nearly 1.5 million AIRS granules in total. From these results, we select measurements at 40-km altitude, near the center of our usable height range, where retrieval noise and cone of influence effects are minimized (Hindley et al., 2019). We then use the background stratospheric temperature $\overline{T}$, our measured temperature perturbation amplitudes T', and zonal, meridional, and vertical wavenumbers k, l, and m to estimate zonal and meridional GWMF MF_x and MF_y as

$$\left(\mathrm{MF}_x, \mathrm{MF}_y\right) = \frac{\rho}{2}\left(\frac{g}{N}\right)^2 \left(\frac{T'}{\overline{T}}\right)^2 \left(\frac{k}{m}, \frac{l}{m}\right) \tag{1}$$

where ρ is density, g is gravitational acceleration, and N is the Brunt-Väisälä frequency (Ern et al., 2004). This relation is valid for hydrostatic and nonrotational GWs and is derived in Ern et al. (2004) under the midfrequency approximation, where the GW intrinsic frequency $\hat{\omega}$ lies in the range $f \ll \hat{\omega} \ll N$, where f is the inertial frequency (e.g., Fritts & Alexander, 2003). (Ern et al., 2017, their supporting information) showed that this relation was valid for waves visible to AIRS. Although no single instrument can observe the full GW spectrum, AIRS is sensitive to relatively long vertical wavelengths and relatively short

horizontal wavelengths (see Figure S1), which can correspond to large GWMF for a given temperature amplitude T' via Equation 1.

To mitigate retrieval noise effects, we follow Ern et al. (2017) and set locations with amplitudes $T' < 0.4$ K to zero. As found by Ern et al. (2017), we see no significant difference in global GWMF distribution if this condition is applied. This suggests that GWMF in the AIRS observational band is dominated by large-amplitude waves.

2.3. Observed Distributions of GWs in AIRS

As is the case for all observational studies of GWs, the distribution of GWMF that we measure in AIRS is primarily the result of three factors: (1) the true distribution of GW sources and propagation in the atmosphere; (2) filtering and/or refraction of GWs by the background winds; and (3) the observational filter.

Factors (1) and (2) are geophysical properties of the atmospheric system. Factor (3) is a property of the AIRS observing system. The AIRS observational filter is quantified in Figure S1 in the supporting information. To help constrain the effects of (2), we also include zonal and meridional winds from European Centre for Medium-Range Weather Forecasts (ECMWF) ERA5 reanalysis (Copernicus Climate Change Service, 2017) near 40-km altitude for all GWMF results in this study.

The interplay between these three factors gives rise to the distributions of AIRS GWMF measurements presented here. By quantifying the measured GWMF in AIRS measurements, which are subject to factors (1–3) above, we can provide useful constraints for GWMF in global models. If factors (1) and (2) are realistically simulated in models, and we apply factor (3), the distributions of resolved GWs in models can be directly compared with the results presented here. Further, our directional GWMF results can provide insight into GW behavior and propagation that can help to guide future parameterizations of unresolved GWs.

3. Results

3.1. Zonal-Mean GW Momentum Fluxes

Figure 1 shows zonal-mean zonal and meridional GWMF near 40 km altitude. Panels (a) and (b) show composite monthly means for 2002–2019, while panels (c) and (d) show daily zonal-mean values. A 30-day running mean is applied to panels (b) and (c).

Composite monthly-mean AIRS GWMF in Figures 1a and 1b reveal large westward fluxes during winter in both hemispheres at middle to high latitudes, with weaker eastward flux in the tropics during summer. An asymmetric zonal flux pattern is seen between the two hemispheres, with average Southern Hemisphere (SH) values nearly twice as large as conjugate months in the Northern Hemisphere (NH) during winter and summer. Wintertime SH zonal fluxes also peak slightly later in the season than in the NH, with the largest westward values of around −2.5 mPa and −1 mPa seen in July and December, respectively.

Meridional GWMF results in Figure 1b also show a striking interhemispheric asymmetry. During austral winter, meridional GWMF converges toward latitudes near 60°S, with large northward (southward) fluxes observed to the south (north). This phenomenon is not seen in NH winter, where zonal-mean GWMF is consistently northward at mid to high latitudes. This GWMF convergence during austral winter, and its representation in GCMs, is currently the topic of active research (Hindley et al., 2015, 2019; Kalisch et al., 2014; Preusse et al., 2014; Sato et al., 2012; Wright et al., 2017). The oblique, or lateral, propagation of GWs is not currently included in most GW parameterizations, which typically assume only columnar GW propagation and momentum deposition.

Figures 1c and 1d show zonal-mean zonal and meridional GWMF against latitude and time. The annual cycle of large westward fluxes at mid to high latitudes during winter and weaker eastward fluxes in the tropics during summer repeats consistently each year. This pattern is strongly regular in the SH, likely due to the relative strength and stability of the southern polar vortex, which allows GWs to propagate and be refracted to long vertical wavelengths visible to AIRS. Indeed, the seasonality of AIRS zonal-mean zonal GWMF in Figure 1c corresponds strongly to the seasonality of zonal-mean zonal winds at 3 hPa shown in Figure S2 in the supporting information. Disruption of the SH vortex by stratospheric planetary wave (PW) activity is much less significant than in the NH, due to the reduced longitudinal ocean-continent contrast at southern high latitudes that drives PW activity in the NH (e.g., Pawson & Kubitz, 1996). At northern

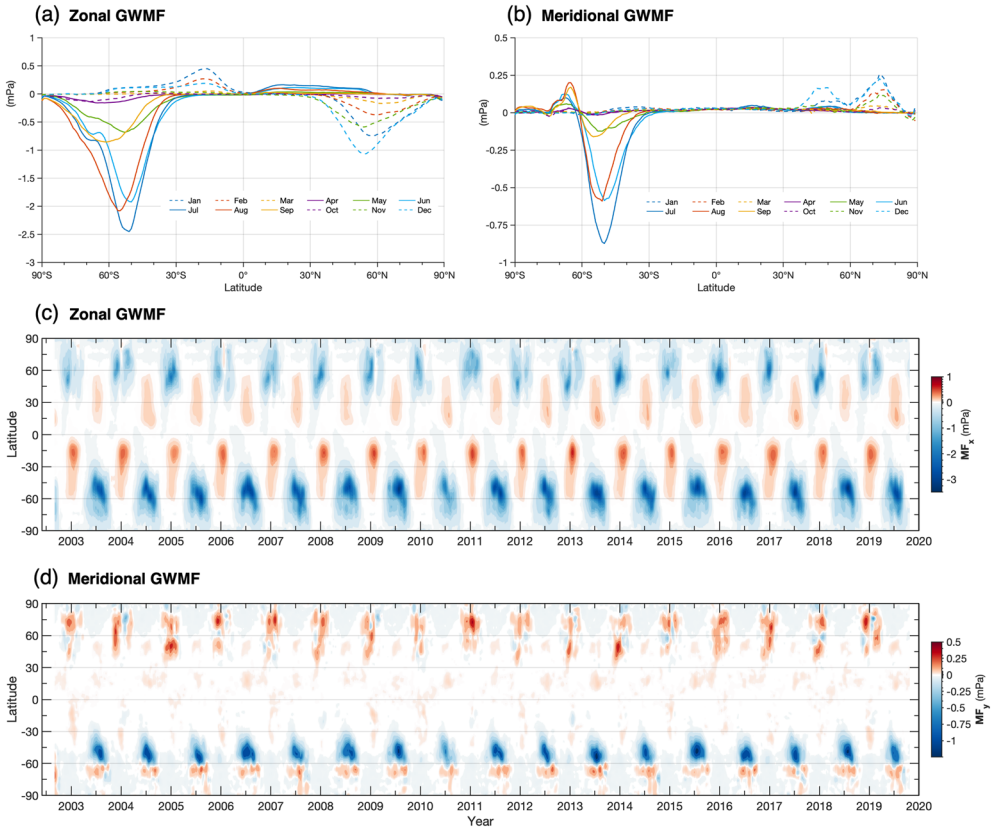

Figure 1. Zonal-mean zonal (a, c) and meridional (b, d) gravity wave momentum flux (GWMF) MF_x and MF_y derived from AIRS/Aqua satellite observations near 40-km altitude for the period 2002–2019. Panels (a) and (b) show composite monthly-mean zonal-mean GWMF against latitude for all years, while panels (c) and (d) show the zonal-mean GWMF against latitude and time. A 30-day running mean is been applied in (c) and (d). For zonal (meridional) GWMF, positive/negative values indicate an eastward/westward (northward/southward) direction.

high latitudes during boreal winter, dramatic reductions and even reversals are found to occur during 2004, 2006, 2009, and 2019. As discussed in section 3.3, these coincide with sudden stratospheric warming (SSW) events, where zonal-mean zonal winds are rapidly reduced. Despite the effect of the AIRS observational filter however, the annual distribution, direction and seasonality of zonal GWMF in our results is in good general agreement with recent high-resolution modeling studies (Sato et al., 2012; S. P. Alexander et al., 2016; Watanabe et al., 2008).

Interestingly, the convergence of meridional GWMF toward 60°S during austral winter occurs each year in Figure 1d. The NH has no clear counterpart to this, with wintertime meridional fluxes directed northward at around 50°N and 70°N during most years. We also find that meridional GWMF during major SSW events in the NH can also briefly reverse from northward to southward, most notably in 2004 and 2019, in addition to the reversal of zonal GWMF from westward to eastward.

3.2. Long-Timescale GWMF Variability at High Latitudes and in the Tropics

Figure 2 shows zonal-mean zonal GWMF at middle to high latitudes in both hemispheres between latitudes of 30–80° (a and c) and in the tropics between ±30° of the equator (b). Also shown are zonal-mean zonal winds from ERA5 reanalysis at 3 and 10 hPa (~40 km and ~30 km altitude, respectively) at 60°N (a), in the tropics between ±30° (b) and at 60°S (c).

An annual cycle in zonal GWMF is observed at mid to high latitudes, while in the tropics we find both an annual and semiannual cycle. In general, the variability and direction of zonal GWMF shows a strong anticorrelation with the zonal wind, especially at high latitudes in Figures 2a and 2c. The Pearson linear correlation coefficient R between the zonal GWMF and zonal wind at 3 hPa is $R_{3\,\mathrm{hPa}} = -0.83$ and $R_{3\,\mathrm{hPa}} = -0.86$ for

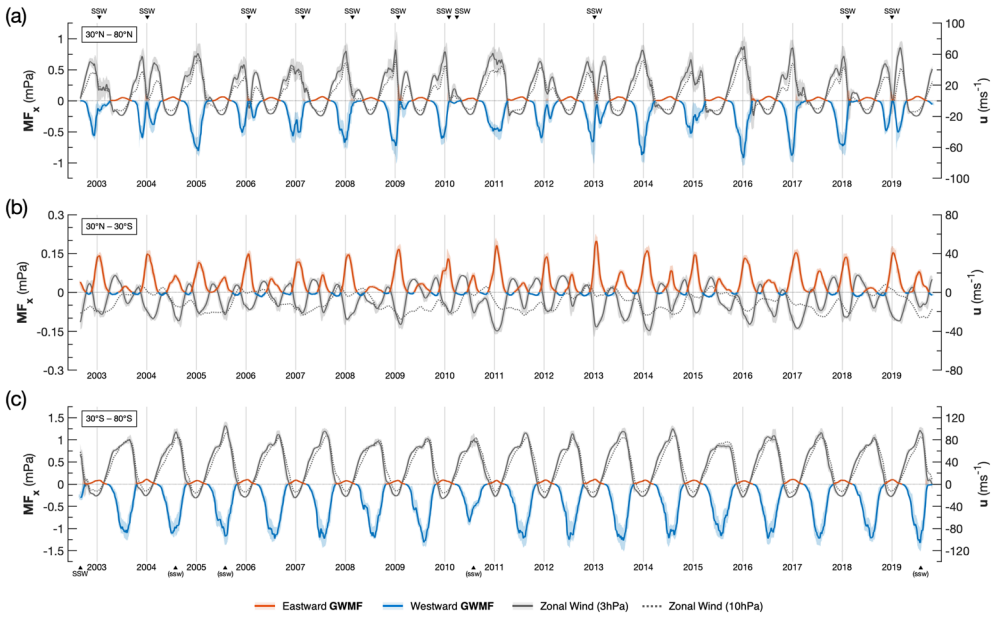

Figure 2. Time series of zonal-mean westward (blue) and eastward (orange) GWMF at 40 km altitude derived from AIRS satellite observations for the latitude bands 30–80°N (a), 30–30°S (b), and 30–80°S (c). Solid and dashed gray lines on each panel show zonal-mean zonal winds from ERA5 reanalysis (right hand axis) at 3 hPa (~40 km) and 10 hPa (~30 km), respectively, at 60°N (a), between ±30° of the equator (b) and at 60°S (c). For all data, solid lines show a 30-day running mean, while shaded regions show ±1 standard deviation of daily zonal-mean values in a running 30-day window. The dates of major and minor sudden stratospheric warming events are marked (SSW) and (ssw) respectively for the Northern (a) and Southern (c) Hemispheres.

the northern and southern high latitudes, respectively. This suggests a significant role for GW filtering and refraction by the background wind. In strong zonal winds, GWs are refracted to long λ_Z, which both increases their GWMF via Equation 1and their visibility within the AIRS observational filter. The negative sign of this correlation suggests that observed GWs in AIRS preferentially propagate against the background wind at high latitudes, as was also found by Ern et al. (2017). Because our assumption of only upward propagation here produces realistic horizontal directionality, this suggests that general assumptions of upwind or upward propagation for most GWs at mid to high latitudes in AIRS measurements may be equally valid.

In the tropics, annual and semiannual cycles are observed in AIRS GWMF in Figure 2b, although the directionis almost always eastward. The zonal-mean tropical GWMF is anticorrelated with the zonal-mean zonal winds at 3 hPa ($R_{3\,\mathrm{hPa}} = -0.76$). The negative sign of this correlation is indicative of strong modulation of GWs by the semiannual oscillation (SAO) in the tropical middle and upper stratosphere (e.g., Smith et al., 2017).

Tropical zonal GWMF in Figure 2b is consistently larger during austral summer than in boreal summer each year. Interestingly, this appears to be the case even in years when the westward phase of the SAO during austral summer is weaker than (or comparable to) the westward phase during boreal summer, such as during 2004 to 2007. This suggests that, in these AIRS measurements, eastward propagating summertime GW activity in the SH is more intense than in the NH. Global maps of AIRS summertime GWMF (see supporting information Figure S4) show that this corresponds to geographic regions of deep convection over South America, Southern Africa, and Southeast Asia, the regional distribution of which is consistent with previous studies (e.g., Alexander et al., 2008; Ern et al., 2017; Ern & Preusse, 2012; Hoffmann & Alexander, 2010; Gong et al., 2015; Sato et al., 2012). In the NH, increased summertime GWMF is found over North America, northern Africa, and East Asia, but seasonal GWMF values are generally smaller than in the corresponding SH regions. These results suggest another possible asymmetry in annual convective GWMF between the hemispheres in AIRS measurements.

The quasi-biennial oscillation (QBO) is seen clearly in the tropical zonal wind at 10 hPa in Figure 2b, where the zonal-mean wind is predominantly westward but reverses to eastward over an approximately 2-year (~28-month) period (e.g., Baldwin et al., 2001). Interestingly, we find that tropical QBO winds at 10 hPa do not appear to modulate observed zonal-mean GWMF above near 3 hPa. Correlation between tropical AIRS GWMF near 3 hPa and the 10 hPa wind in Figure 2b is very low, with $R_{10\,\mathrm{hPa}} = -0.09$. Correlation between AIRS GWMF and the tropical zonal wind at 40 hPa, where the QBO periodicity is most clearly seen (Baldwin et al., 2001), yields an even lower correlation with $R_{40\,\mathrm{hPa}} = 0.04$. Reducing the latitudinal range of the AIRS GWMF and/or zonal winds to ±10° around the equator, or directly over the equator, made no significant difference to these correlation values. To investigate further, Lomb-Scargle spectral analysis (Lomb, 1976; Scargle, 1982) of the tropical zonal GWMF in Figure 2b was performed (see supporting information Figure S3). Strong annual and semiannual periodicity was found, as seen clearly in Figure 2b, but no significant periodicity near 28 months could be found in tropical AIRS GWMF.

Despite the important role that tropical GWs can play in the QBO (e.g., Kawatani et al., 2010), this null result is not unexpected. Using limb-sounding satellite observations, which have a higher vertical resolution than AIRS, Ern et al. (2014) found that only GWs with vertical wavelengths $\lambda_z \lesssim 10$ km interacted significantly with the QBO. Here, AIRS is primarily sensitive to GWs with $\lambda_z \gtrsim 15$ km, so our result of no significant QBO periodicity in AIRS GWMF at these longer vertical wavelengths is consistent with the results of Ern et al. (2014). Further, Anstey et al. (2016) found that only GCMs with vertical resolutions $\lesssim$ 1 km in the tropical lower stratosphere, such that GWs with short vertical wavelengths could be resolved, were able to simulate a realistic QBO. Our results are therefore consistent with the hypothesis that only GWs with $\lambda_z \lesssim 10$ km exhibit a significant interaction with the QBO.

3.3. GWMF Variability During SSW Events

The dates of major SSWs in both hemispheres are indicated in Figures 2a and 2c. These dates are obtained from Butler et al. (2017), following the definition of Charlton and Polvani (2007), where the daily zonal-mean zonal winds at 60°N at 10 hPa must turn westerly for at least 10 days prior to 30 April. In the SH, the date of the 2002 major SSW (Allen et al., 2003; Baldwin et al., 2003; Charlton et al., 2005) using the conjugate definition is shown. Suspected SH minor SSWs in 2004, 2005, and 2010 (Chandran et al., 2014; Eswaraiah et al., 2016) and 2019 (Rao et al., 2020) are also shown. The minor SSW dates are approximate, since there is currently no universally agreed definition for these (Butler et al., 2015).

Significant disruptions to the wintertime GWMF during SSWs are observed in Figure 2a, where zonal GWMF rapidly reduces and occasionally reverses during the 2004, 2006, 2013, and 2019 major SSWs, closely following reductions and reversals in the zonal wind at 3 hPa. This suggests that a large fraction of observed westward wintertime GWMF may be westward propagating tropospheric orographic waves, which are prevented from ascending during SSWs. The reversals of zonal GWMF are consistent with the behavior of parameterized GWs in modeling studies (Hitchcock & Shepherd, 2013; Polichtchouk et al., 2018), but to our knowledge they have not been well-studied in observations before now.

This variability is not seen in the SH in Figure 2c. Instead, the SH exhibits the strongest anticorrelation between zonal GWMF and the seasonal winds at 3 hPa ($R_{3\,\mathrm{hPa}} = -0.86$). Here, a sawtooth pattern is found in both the zonal flux and wind speed, which increase throughout autumn into winter followed by a sudden reduction in spring. This pattern is strongly suggestive of an important role for filtering and refraction of GWs by the background winds. The only significant exception is found during 2010 where, despite the zonal-mean winds being relatively similar to other years, zonal-mean GWMF reduces by nearly 50% from the climatological mean. This coincides with minor SSW in the SH (e.g., Chandran et al., 2014; Eswaraiah et al., 2016), which suggests that the position and stability of the polar night jet also plays a significant role in the observed GWMF in AIRS at southern high latitudes. Significant disruption to the SH wintertime GWMF may also have occurred during the 2002 major SSW, although we note that this event took place just outside of the time range shown here.

3.4. Geographic Distribution of Wintertime GWMF in the NH and SH

For our final investigation, we quantify long-time average stratospheric wintertime GWMF in AIRS measurements over geographic "hot spots" in both hemispheres. Figure 3 shows composite wintertime zonal and meridional GWMF for the NH and SH for 2002–2019. Panels (a)–(d) show zonal (top row) and

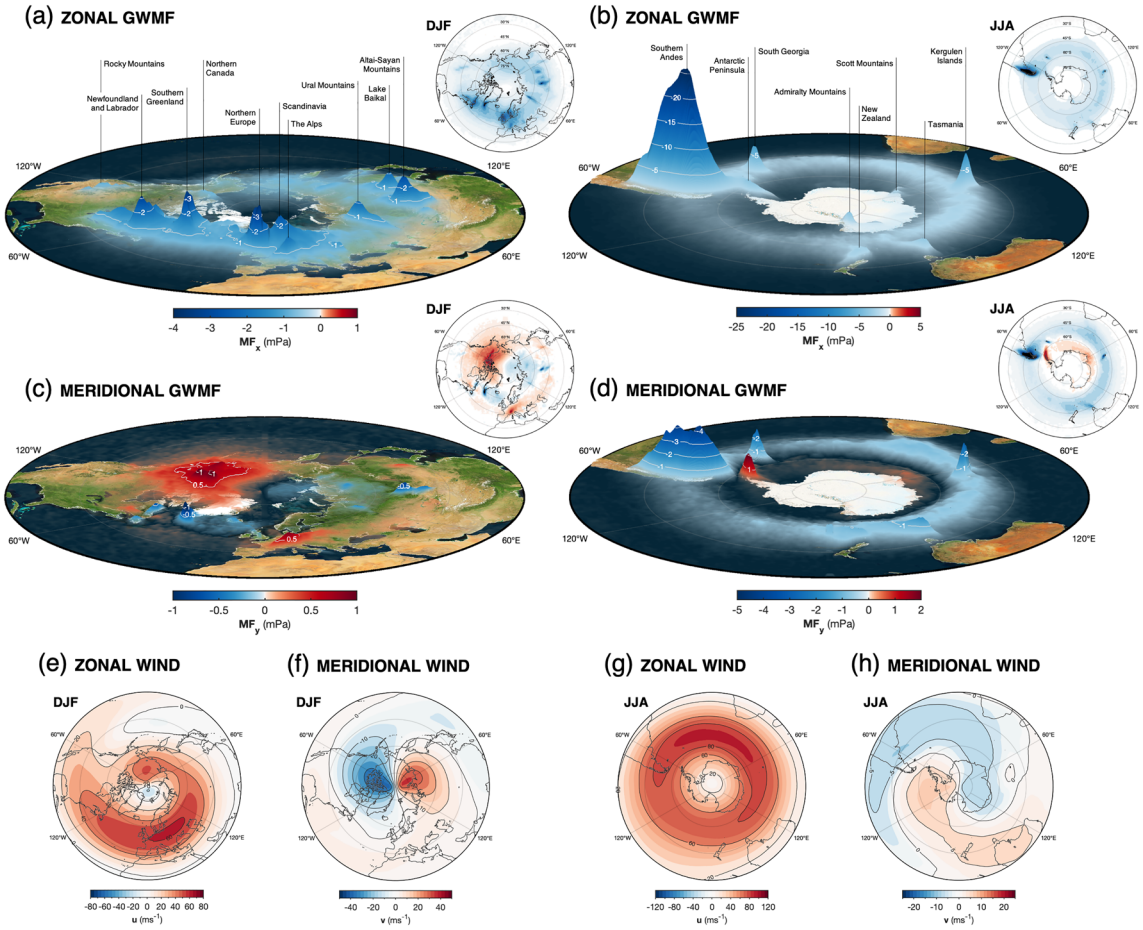

Figure 3. Stereographic maps of average wintertime zonal (a, b) and meridional (c, d) GWMF near 40 km altitude derived from AIRS observations for the period 2002–2019. Winter is defined as December–February (June–August) for the Northern (Southern) Hemisphere. GWMF values that are close to zero have been made transparent to reveal the surface features below, and landmarks that lie beneath regions of increased GWMF have been labeled. Inset in the top right of each panel is a stereographic map of the same data but centered on the north and south poles. These inset panels share a color scale with the corresponding 3-D contours. Panels (e)–(h) show average wintertime zonal and meridional winds at 3 hPa for the period 2002–2019 from ERA5 reanalysis.

meridional (middle row) GWMF during boreal winter and austral winter. Zonal and meridional fluxes in Figures 3a–3d are shown as 3-D contour surfaces, where the height corresponds to the GWMF magnitude and color denotes direction. Height is used to make the relative magnitudes of the GW hot spots clearer. Insets to the top right of panels (a)–(d) show the same data but centered at the north and south poles. Lastly, panels (e)–(h) show average wintertime zonal and meridional winds at 3 hPa from ERA5 reanalysis for the same period.

In the NH, hot spots of increased zonal GWMF are found over North America, Europe and Asia in Figure 3a, with seasonal-mean values near 3 mPa. These hot spots are generally located over mountainous regions, where strong wintertime zonal winds allow mountain waves to propagate vertically and refract to the long vertical wavelengths visible to AIRS. The multiyear analysis here will also favor such hot spots because the mountains are in the same location each year, whereas nonorographic wave sources such as storms, fronts and jet imbalance are transitory phenomena. The geographic distribution of GW activity is in close agreement with other studies of GW hot spots in AIRS measurements (e.g., Hoffmann et al., 2013).

The largest hot spots of zonal GWMF in the NH lie over Newfoundland and Labrador and northern Europe, centered over the United Kingdom. The United Kingdom has preferential conditions for orographic GW generation, where surface winds have a long path over the oceans before encountering mountainous terrain (e.g., Bacmeister, 1993). Both these locations also lie under regions of significant variability in the latitudinal

position of the upper tropospheric jet, which could result in increased measurement of nonorographic waves over these regions from spontaneous adjustment processes in the jet exit region (e.g., Bossert et al., 2020; Krisch et al., 2020; O'Sullivan & Dunkerton, 1995).

In the SH, the GWMF hot spot over the southern Andes dominates the wintertime distribution, with seasonal-mean westward GWMF exceeding 25 mPa. Here, the combination of strong tropospheric wind flow over the mountains of the southern Andes and the strong stratospheric winds of the southern polar vortex usually results in the largest single hot spot of stratospheric GWMF measured on Earth (e.g., Ern et al., 2004; Geller et al., 2013; Hoffmann et al., 2013, 2016; Yan et al., 2010). The southern wintertime polar vortex is tightly localized around 60°S, with seasonal-mean winds exceeding 80 ms^{-1} (Figure 3g). This structure is relatively unperturbed by topographically forced planetary wave activity, unlike in the NH. These factors provide ideal conditions for the propagation of mountain waves into the stratosphere and higher during winter (e.g., Kaifler et al., 2020; Liu et al., 2019).

These wind conditions can also result in large measured GWMF values over small isolated mountainous islands in the Southern Ocean, such as South Georgia and Kerguelen in Figure 3b, where peak seasonal-mean zonal GWMF values exceeding 5 mPa are larger than over any single location in the NH. This is despite significantly more land and mountainous topography in the NH. Quantifying the impact of GWMF from these islands on the stratospheric circulation is a topic of active research (Alexander & Grimsdell, 2013; Hindley et al., 2020; Jackson et al., 2018; Vosper, 2015), since they lie in the "gray zone" of model resolution, where they are neither fully resolved nor fully parameterized (Vosper, 2015; Vosper et al., 2016). Additional regions of increased stratospheric zonal GWMF in Figure 3b are found over the Antarctic Peninsula, New Zealand, Tasmania, and mountain ranges on the Antarctic coast, the locations of which are in good agreement with previous studies (Hindley et al., 2019; Hoffmann et al., 2013, 2016).

The geographical distribution of meridional GWMF in Figures 3c and 3d also presents an interesting picture. Wintertime hot spots in the NH show a strong anticorrelation with seasonal-mean meridional winds in Figure 3f, where a striking region of northward GWMF is found over northern Canada. This feature is in good agreement with the results of Ern et al. (2017), who found northward GWMF over northern Canada and southward GWMF over Siberia in AIRS measurements during January 2009. Meridional winds in Figure 3f are anticorrelated with the meridional GWMF distribution found in Figure 3c, again suggesting an important role for GW filtering in the NH by stratospheric meridional winds. The prominent dipole-like distribution of the meridional wind in the NH could be the result of the long-time average shown here, where the northward and southward nodes of planetary wave activity in the stratosphere are often geographically consistent each year (e.g., Kleinknecht et al., 2014).

In the SH, the distribution of meridional GWMF in Figure 3d shows a clear convergence of GWMF toward latitudes near 60°S, with northward (southward) GWMF located to the south (north) (Hindley et al., 2015, 2019; Preusse et al., 2014; Sato et al., 2012). In contrast to our results in the NH, this does not appear to correspond to GW propagation against the background meridional winds in Figure 3h. The most significant example of this convergence of GWMF is found over the Drake Passage at around 60°W, where southward flux over the southern Andes and northward flux over Antarctic Peninsula converges toward 60°S. This directionality may be the result of a strong latitudinal gradient in zonal wind speed either side of the stratospheric jet, as shown in Figure 3g (e.g., Dunkerton, 1984; Sato et al., 2012). For zonally propagating GWs that form to the north and south, this latitudinal wind gradient could behave like a classical waveguide, refracting waves toward the center of the jet.

Such behavior is not generally included in columnar GW parameterizations, since the horizontal gradient of the background wind is not considered (Plougonven et al., 2020). Our results could therefore be significant for the long-standing cold-pole bias in GCMs that is suspected to arise due to a lack of GW drag near 60°S (Butchart et al., 2011). The lateral propagation of GWMF could thus provide an important part of this "missing flux" near 60°S that could be considered in future parameterization schemes (Kalisch et al., 2014).

Lastly, a "belt" of increased GWMF located around 60°S over the Southern Ocean is observed in Figures 3b and 3d. The precise source of this belt of enhanced GW activity has been unclear since its discovery in early satellite observations (e.g., Alexander et al., 2008; Wu, 2004; Wu & Waters, 1996; Yan et al., 2010), prompting specific investigations (e.g., Hendricks et al., 2014; Hindley et al., 2015).

Hindley et al. (2019) found that in the latitude band 35°S to 68°S during June–August 2010, only approximately 30% of the total GWMF was found between longitudes of 55°W to 80°W over the southern Andes and Antarctic Peninsula. The remaining 70% of the measured GWMF found was at other longitudes over the Southern Ocean. If we repeat the approach of Hindley et al. (2019) here but for average GWMF for all austral winters (June–August) for the period 2002–2019, we find only 25.4% of the total GWMF over the southern Andes and Antarctic Peninsula sector and 74.6% over the Southern Ocean.

The absence of major orography suggests a nonorographic origin for these waves, such as from storms (S. P. Alexander et al., 2016; Choi & Chun, 2013; Jewtoukoff et al., 2015), fronts (Plougonven & Zhang, 2014), baroclinic instabilities in the troposphere (e.g., O'Sullivan & Dunkerton, 1995), or excitation of waves around the polar vortex edge (Polichtchouk & Scott, 2020). It has also been suggested that small mountainous islands in the Southern Ocean might make up a significant portion of the oceanic GWMF near 60°S (Garfinkel & Oman, 2018; McLandress et al., 2012). Our results in Figure 3b however show that although GWMF hot spots are found over some islands, significant GWMF is also found over open ocean, suggesting GWMF from small islands might not complete the whole picture.

4. Conclusions

In this study, global measurements of stratospheric GWs from AIRS/Aqua observations are analysed for the period 2002–2019. Using a 3-D *S*-transform method, a global climatology of directional zonal and meridional GWMF near 40 km altitude is presented for GWs with $\lambda_z \gtrsim 15$ km and $\lambda_H \lesssim 800$ km. For the first time, the distribution and interannual variability of directional stratospheric GWMF in AIRS observations is quantified over nearly two decades of data. Our conclusions are as follows:

1. A clear annual cycle of stratospheric GWMF is found at middle and high latitudes, with large westward GWMF in winter and weaker eastward GWMF in summer. Measured zonal-mean zonal GWMF in AIRS is around 2× larger in the Southern Hemisphere than in the north during both winter and summer. The magnitude and direction of this zonal GWMF correlates strongly with the background zonal wind, suggesting an important role for refraction and filtering of GWs by the background winds.
2. The most significant disruptions to the annual cycle of GWMF at high latitudes occur during SSW events in both hemispheres, where dramatic reductions and even reversals of zonal-mean GWMF are found in the Northern Hemisphere. This result is consistent with recent studies of parameterized GWs in models (Hitchcock & Shepherd, 2013; Polichtchouk et al., 2018).
3. In the tropics, we find strong modulation of the observed AIRS GWMF by the semiannual oscillation (SAO), but no significant modulation by the QBO. This result is consistent with the results of Ern et al. (2014) and Anstey et al. (2016) that suggest only tropical GWs with short vertical wavelengths ($\lambda_z \lesssim 10$ km), which are invisible to AIRS, that exhibit a significant interaction with the QBO.
4. The largest single hot spot of measured GWMF is found over the southern Andes during austral winter, where values are more than 10 times larger than any other location on Earth. Despite this, we find that nearly 75% of the total wintertime GWMF at latitudes near 60°S is actually found over the Southern Ocean.
5. A meridional convergence of GWMF toward the center of the stratospheric jet near 60°S is observed each year in the Southern Hemisphere. This has no counterpart in the northern hemisphere. This effect, which is not considered in most GW parameterizations, has significance for the long-standing cold-pole bias in GCMs.

These results provide a global insight into the distribution and behavior of GWs in AIRS observations of the middle atmosphere. By quantifying the magnitude and constraining the direction of stratospheric GWMF in AIRS measurements over nearly two decades, we provide quantitative values to which simulated GWMF in models can be compared. We have also gained new understanding of the interannual variability and lateral propagation effects stratospheric GWs. Our results will help to guide the development of future GW parameterizations and test resolved GWs in global models, leading to more accurate simulations of dynamics, circulations and ultimately better forecasts of weather and climate.

Data Availability Statement

The AIRS temperature data set is derived using AIRS radiances freely available from NASA's GES DISC at https://disc.gsfc.nasa.gov/ website. These radiances are then processed as described in Hoffmann and Alexander (2009).

Acknowledgments
This study is supported by the U.K. Natural Environment Research Council (NERC) under grant numbers NE/R001391/1 and NE/R001235/1 supporting N. P. Hindley, C. J. Wright, N. J. Mitchell, and T. Moffat-Griffin and by a Royal Society University Research Fellowship UF160545 supporting C. J. W. The authors gratefully acknowledge the BALENA high-performance computing service at the University of Bath, the JURECA high-performance computing service at Forschungszentrum Jülich and the ERA5 reanalysis data set available from the Copernicus Climate Data Store (C3S) at the European Centre for Medium-Range Weather Forecasts (ECMWF). We would like to thank Dann Mitchell for helpful discussions on SSWs and Joan Alexander for discussions on the observational filter. Finally, we would like to thank Inna Polichtchouk and one anonymous reviewer for their helpful comments and suggestions.

References

Alexander, M. J. (1998). Interpretations of observed climatological patterns in stratospheric gravity wave variance. *Journal of Geophysical Research*, *103*(D8), 8627–8640. https://doi.org/10.1029/97JD03325

Alexander, M. J. (2015). Global and seasonal variations in three-dimensional gravity wave momentum flux from satellite limb-sounding temperatures. *Geophysical Research Letters*, *42*, 6860–6867. https://doi.org/10.1002/2015GL065234

Alexander, M. J., & Barnet, C. (2007). Using satellite observations to constrain parameterizations of gravity wave effects for global models. *Journal of the Atmospheric Sciences*, *64*, 1652–1665. https://doi.org/10.1175/JAS3897.1

Alexander, M. J., Eckermann, S. D., Broutman, D., & Ma, J. (2009). Momentum flux estimates for South Georgia Island mountain waves in the stratosphere observed via satellite. *Geophysical Research Letters*, *36*, L12816. https://doi.org/10.1029/2009GL038587

Alexander, M. J., Geller, M., McLandress, C., Polavarapu, S., Preusse, P., Sassi, F., et al. (2010). Recent developments in gravity-wave effects in climate models and the global distribution of gravity-wave momentum flux from observations and models. *Quarterly Journal of the Royal Meteorological Society*, *136*(650, A), 1103–1124. https://doi.org/10.1002/qj.637

Alexander, M. J., Gille, J., Cavanaugh, C., Coffey, M., Craig, C., Eden, T., et al. (2008). Global estimates of gravity wave momentum flux from high resolution dynamics limb sounder observations. *Journal of Geophysical Research*, *113*, D15S18. https://doi.org/10.1029/2007JD008807

Alexander, M. J., & Grimsdell, A. W. (2013). Seasonal cycle of orographic gravity wave occurrence above small islands in the Southern Hemisphere: Implications for effects on the general circulation. *Journal Geophysical Research: Atmospheres*, *118*, 11,589–11,599. https://doi.org/10.1002/2013JD020526

Alexander, S. P., Sato, K., Watanabe, S., Kawatani, Y., & Murphy, D. J. (2016). Southern hemisphere extratropical gravity wave sources and intermittency revealed by a Middle-Atmosphere general circulation model. *Journal of the Atmospheric Sciences*, *73*(3), 1335–1349. https://doi.org/10.1175/JAS-D-15-0149.1

Allen, D. R., Bevilacqua, R. M., Nedoluha, G. E., Randall, C. E., & Manney, G. L. (2003). Unusual stratospheric transport and mixing during the 2002 antarctic winter. *Geophysical Research Letters*, *30*(12), 1599. https://doi.org/10.1029/2003GL017117

Anstey, J. A., Scinocca, J. F., & Keller, M. (2016). Simulating the QBO in an atmospheric general circulation model: Sensitivity to resolved and parameterized forcing. *Journal of the Atmospheric Sciences*, *73*(4), 1649–1665. https://doi.org/10.1175/jas-d-15-0099.1

Aumann, H. H., Chahine, M. T., Gautier, C., Goldberg, M. D., Kalnay, E., McMillin, L. M., et al. (2003). AIRS/AMSU/HSB on the aqua mission: Design, science objectives, data products, and processing systems. *IEEE Transactions on Geoscience and Remote Sensing*, *41*(2), 253–264. https://doi.org/10.1109/TGRS.2002.808356

Bacmeister, J. T. (1993). Mountain-Wave drag in the stratosphere and mesosphere inferred from observed winds and a simple Mountain-Wave parameterization scheme. *Journal of the Atmospheric Sciences*, *50*(3), 377–399. https://doi.org/10.1175/1520-0469(1993)050<0377:MWDITS>2.0.CO;2

Bacmeister, J. T., & Schoeberl, M. R. (1989). Breakdown of vertically propagating two-dimensional gravity waves forced by orography. *Journal of the Atmospheric Sciences*, *46*, 2109–2134.

Baldwin, M. P., Gray, L. J., Dunkerton, T. J., Hamilton, K., Haynes, P. H., Randel, W. J., et al. (2001). The quasi-biennial oscillation. *Reviews of Geophysics*, *39*(2), 179–229. https://doi.org/10.1029/1999RG000073

Baldwin, M. P., Hirooka, T., O'Neill, A., & Yoden, S. (2003). Major stratospheric warming in the southern hemisphere in 2002: Dynamical aspects of the ozone hole split. *SPARC Newsletter*, *20*, 24–26.

Becker, E., & Vadas, S. L. (2018). Secondary gravity waves in the winter mesosphere: Results from a high-resolution global circulation model. *Journal of Geophysical Research: Atmospheres*, *123*, 2605–2627. https://doi.org/10.1002/2017JD027460

Bossert, K., Kruse, C. G., Heale, C. J., Fritts, D. C., Williams, B. P., Snively, J. B., et al. (2017). Secondary gravity wave generation over New Zealand during the DEEPWAVE campaign. *Journal of Geophysical Research: Atmospheres*, *122*, 7834–7850. https://doi.org/10.1002/2016JD026079

Bossert, K., Vadas, S. L., Hoffmann, L., Becker, E., Harvey, V. L., & Bramberger, M. (2020). Observations of stratospheric gravity waves over Europe on 12 January 2016: The role of the polar night jet. *Journal of Geophysical Research: Atmospheres*, *125*, e2020JD032893. https://doi.org/10.1029/2020JD032893

Butchart, N., Charlton-Perez, A. J., Cionni, I., Hardiman, S. C., Haynes, P. H., Krüger, K., et al. (2011). Multimodel climate and variability of the stratosphere. *Journal Geophysical Research*, *116*, D05102. https://doi.org/10.1029/2010JD014995

Butler, A. H., Seidel, D. J., Hardiman, S. C., Butchart, N., Birner, T., & Match, A.(2015). Defining sudden stratospheric warmings. *Bulletin of the American Meteorological Society*, *96*(11), 1913–1928. https://doi.org/10.1175/BAMS-D-13-00173.1

Butler, A. H., Sjoberg, J. P., Seidel, D. J., & Rosenlof, K. H. (2017). A sudden stratospheric warming compendium. *Earth System Science Data*, *9*(1), 63–76. https://doi.org/10.5194/essd-9-63-2017

Chahine, M. T., Pagano, T. S., Aumann, H. H., Atlas, R., Barnet, C., Bblaisdell, J., et al. (2006). AIRS: Improving weather forecasting and providing new data on Greenhouse gases. *Bulletin of the American Meteorological Society*, *87*(7), 911–926. https://doi.org/10.1175/BAMS-87-7-911

Chandran, A., Collins, R. L., & Harvey, V. L. (2014). Stratosphere-mesosphere coupling during stratospheric sudden warming events. *Advances in Space Research*, *53*(9), 1265–1289. https://doi.org/10.1016/j.asr.2014.02.005

Charlton, A. J., O'Neill, A., Lahoz, W. A., & Berrisford, P. (2005). The splitting of the stratospheric polar vortex in the southern hemisphere, september 2002: Dynamical evolution. *Journal of the Atmospheric Sciences*, *62*(3), 590–602. https://doi.org/10.1175/JAS-3318.1

Charlton, A. J., & Polvani, L. M. (2007). A new look at stratospheric sudden warmings. Part I: Climatology and modeling benchmarks. *Journal of Climate*, *20*(3), 449–469. https://doi.org/10.1175/JCLI3996.1

Charron, M., Manzini, E., & Warner, C. D. (2002). Intercomparison of gravity wave parameterizations: Hines Doppler-Spread and warner and McIntyre Ultra-Simple schemes. *Journal of the Meteorological Society of Japan. Ser. II*, *80*(3), 335–345. https://doi.org/10.2151/jmsj.80.335

Choi, H.-J., & Chun, H.-Y. (2013). Effects of convective gravity wave drag in the southern hemisphere winter stratosphere. *Journal of the Atmospheric Sciences*, *70*(7), 2120–2136. https://doi.org/10.1175/JAS-D-12-0238.1

Copernicus Climate Change Service (2017). ERA5: Fifth generation of ECMWF atmospheric reanalyses of the global climate. European Centre For Medium-Range Weather Forecasts (ECMWF), https://cds.climate.copernicus.eu/. ([Accessed Dec 2018]).

Dunkerton, T. J. (1984). Inertia-gravity waves in the stratosphere. *Journal of the Atmospheric Sciences*, *41*(23), 3396–3404. https://doi.org/10.1175/1520-0469(1984)041<3396:IWITS>2.0.CO;2

Ern, M., Hoffmann, L., & Preusse, P. (2017). Directional gravity wave momentum fluxes in the stratosphere derived from high-resolution AIRS temperature data. *Geophysical Research Letters*, *44*, 475–485. https://doi.org/10.1002/2016GL072007

Ern, M., Ploeger, F., Preusse, P., Gille, J. C., Gray, L. J., Kalisch, S., et al. (2014). Interaction of gravity waves with the QBO: A satellite perspective. *Journal of Geophysical Research: Atmospheres*, *119*, 2329–2355. https://doi.org/10.1002/2013JD020731

Ern, M., & Preusse, P. (2012). Gravity wave momentum flux spectra observed from satellite in the summertime subtropics: Implications for global modeling. *Geophysical Research Letters*, *39*, L15810. https://doi.org/10.1029/2012GL052659

Ern, M., Preusse, P., Alexander, M. J., & Warner, C. D. (2004). Absolute values of gravity wave momentum flux derived from satellite data. *Journal Geophysical Research*, *109*, D20103. https://doi.org/10.1029/2004JD004752

Eswaraiah, S., Kim, Y. H., Hong, J., Kim, J.-H., Ratnam, M. V., Chandran, A., et al. (2016). Mesospheric signatures observed during 2010 minor stratospheric warming at King Sejong station (62S, 59W). *Journal of Atmospheric and Solar-Terrestrial Physics*, *140*, 55–64. https://doi.org/10.1016/j.jastp.2016.02.007

Faber, A., Llamedo, P., Schmidt, T., de la Torre, A., & Wickert, J. (2013). On the determination of gravity wave momentum flux from GPS radio occultation data. *Atmospheric Measurement Techniques*, *6*, 3169–3180. https://doi.org/10.5194/amt-6-3169-2013

Fritts, D. C., & Alexander, M. J. (2003). Gravity wave dynamics and effects in the middle atmosphere. *Reviews of Geophysics*, *41*(1), 1003. https://doi.org/10.1029/2001RG000106

Fritts, D. C., Vadas, S. L., Wan, K., & Werne, J. A. (2006). Mean and variable forcing of the middle atmosphere by gravity waves. *Journal of Atmospheric and Solar-Terrestrial Physics*, *68*(3), 247–265. (Vertical Coupling in the Atmosphere/Ionosphere System) https://doi.org/10.1016/j.jastp.2005.04.010

Garcia, R. R., Smith, A. K., Kinnison, D. E., de la Camara, A., & Murphy, D. J. (2017). Modification of the gravity wave parameterization in the whole atmosphere community climate model: Motivation and results. *Journal of the Atmospheric Sciences*, *74*(1), 275–291. https://doi.org/10.1175/JAS-D-16-0104.1

Garfinkel, C. I., & Oman, L. D. (2018). Effect of gravity waves from small islands in the southern ocean on the Southern Hemisphere atmospheric circulation. *Journal of Geophysical Research: Atmospheres*, *123*, 1552–1561. https://doi.org/10.1002/2017JD027576

Geller, M., Alexander, M. J., Love, P., Bacmeister, J., Ern, M., Hertzog, A., et al. (2013). A Comparison between gravity wave momentum fluxes in observations and climate models. *Journal of Climate*, *26*, 6383–6405. https://doi.org/10.1175/JCLI-D-12-00545.1

Gong, J., Yue, J., & Wu, D. L. (2015). Global survey of concentric gravity waves in AIRS images and ECMWF analysis. *Journal Geophysical Research: Atmospheres*, *120*, 2210–2228. https://doi.org/10.1002/2014JD022527

Heale, C. J., Bossert, K., Vadas, S. L., Hoffmann, L., Dörnbrack, A., Stober, G., et al. (2020). Secondary gravity waves generated by breaking mountain waves over Europe. *Journal of Geophysical Research: Atmospheres*, *125*, e2019JD031662. https://doi.org/10.1029/2019JD031662

Hendricks, E., Doyle, J., Eckermann, S. D., Jiang, Q., & Reinecke, P. (2014). What is the source of the stratospheric gravity wave belt in austral winter? *Journal of the Atmospheric Sciences*, *71*, 1583–1592. https://doi.org/10.1175/JAS-D-13-0332.1

Hertzog, A., Alexander, M. J., & Plougonven, R. (2012). On the intermittency of gravity wave momentum flux in the stratosphere. *Journal of the Atmospheric Sciences*, *69*, 3433–3448. https://doi.org/10.1175/JAS-D-12-09.1

Hindley, N. P., Smith, N. D., Wright, C. J., Rees, D. A. S., & Mitchell, N. J. (2016). A two-dimensional Stockwell transform for gravity wave analysis of AIRS measurements. *Atmospheric Measurement Techniques*, *9*(6), 2545–2565. https://doi.org/10.5194/amt-9-2545-2016

Hindley, N. P., Wright, C. J., Gadian, A. M., Hoffmann, L., Hughes, J. K., Jackson, D. R., et al. (2020). Stratospheric gravity-waves over the mountainous island of south Georgia: Testing a high-resolution dynamical model with 3-D satellite observations and radiosondes. *Atmospheric Chemistry and Physics*, *2020*, 1–50. https://doi.org/10.5194/acp-2020-465

Hindley, N. P., Wright, C. J., Smith, N. D., Hoffmann, L., Holt, L. A., Alexander, M. J., et al. (2019). Gravity waves in the winter stratosphere over the Southern Ocean: High-resolution satellite observations and 3-D spectral analysis. *Atmospheric Chemistry and Physics*, *19*(24), 15,377–15,414. https://doi.org/10.5194/acp-19-15377-2019

Hindley, N. P., Wright, C. J., Smith, N. D., & Mitchell, N. J. (2015). The southern stratospheric gravity wave hot spot: Individual waves and their momentum fluxes measured by COSMIC GPS-RO. *Atmospheric Chemistry and Physics*, *15*(14), 7797–7818. https://doi.org/10.5194/acp-15-7797-2015

Hitchcock, P., & Shepherd, T. G. (2013). Zonal-mean dynamics of extended recoveries from stratospheric sudden warmings. *Journal of the Atmospheric Sciences*, *70*(2), 688–707. https://doi.org/10.1175/jas-d-12-0111.1

Hoffmann, L., & Alexander, M. J. (2009). Retrieval of stratospheric temperatures from Atmospheric Infrared Sounder radiance measurements for gravity wave studies. *Journal Geophysical Research*, *114*, D07105. https://doi.org/10.1029/2008JD011241

Hoffmann, L., & Alexander, M. J. (2010). Occurrence frequency of convective gravity waves during the north American thunderstorm season. *Journal Geophysical Research*, *115*, D20111. https://doi.org/10.1029/2010JD014401

Hoffmann, L., Alexander, M. J., Clerbaux, C., Grimsdell, A. W., Meyer, C. I., Roessler, T., & Tournier, B. (2014). Intercomparison of stratospheric gravity wave observations with AIRS and IASI. *Atmospheric Measurement Techniques*, *7*(12), 4517–4537. https://doi.org/10.5194/amt-7-4517-2014

Hoffmann, L., Grimsdell, A. W., & Alexander, M. J. (2016). Stratospheric gravity waves at southern hemisphere orographic hotspots: 2003–2014 AIRS/aqua observations. *Atmospheric Chemistry and Physics*, *16*(14), 9381–9397. https://doi.org/10.5194/acp-16-9381-2016

Hoffmann, L., Xue, X., & Alexander, M. J. (2013). A global view of stratospheric gravity wave hotspots located with Atmospheric Infrared Sounder observations. *Journal Geophysical Research: Atmospheres*, *118*, 416–434. https://doi.org/10.1029/2012JD018658

Hu, S., Ma, S., Yan, W., Hindley, N. P., Xu, K., & Jiang, J. (2019). Measuring gravity wave parameters from a nighttime satellite Low-Light image based on Two-Dimensional Stockwell transform. *Journal of Atmospheric and Oceanic Technology*, *36*(1), 41–51. https://doi.org/10.1175/JTECH-D-18-0092.1

Hu, S., Ma, S., Yan, W., Hindley, N. P., & Zhao, X. (2019). Measuring internal solitary wave parameters based on VIIRS/DNB data. *International Journal of Remote Sensing*, *0*(0), 1–12. https://doi.org/10.1080/01431161.2019.1608389

Jackson, D. R., Gadian, A., Hindley, N. P., Hoffmann, L., Hughes, J., King, J., et al. (2018). The south Georgia wave experiment: A means for improved analysis of gravity waves and Low-Level wind impacts generated from mountainous islands. *Bulletin of the American Meteorological Society*, *99*(5), 1027–1040. https://doi.org/10.1175/BAMS-D-16-0151.1

Jewtoukoff, V., Hertzog, A., Plougonven, R., de la Camara, A., & Lott, F. (2015). Comparison of gravity waves in the southern hemisphere derived from balloon observations and the ECMWF analyses. *Journal of the Atmospheric Sciences*, *72*(9), 3449–3468. https://doi.org/10.1175/JAS-D-14-0324.1

Kaifler, N., Kaifler, B., Dörnbrack, A., Rapp, M., Hormaechea, J. L., & de la Torre, A. (2020). Lidar observations of large-amplitude mountain waves in the stratosphere above Tierra del Fuego, Argentina. *Scientific Reports*, *10*(1), 14529. https://doi.org/10.1038/s41598-020-71443-7

Kalisch, S., Preusse, P., Ern, M., Eckermann, S. D., & Riese, M. (2014). Differences in gravity wave drag between realistic oblique and assumed vertical propagation. *Journal of Geophysical Research: Atmospheres*, *119*, 10,081–10,099. https://doi.org/10.1002/2014JD021779

Kawatani, Y., Watanabe, S., Sato, K., Dunkerton, T. J., Miyahara, S., & Takahashi, M. (2010). The roles of equatorial trapped waves and internal Inertia-Gravity waves in driving the Quasi-Biennial oscillation. Part I: Zonal mean wave forcing. *Journal of the Atmospheric Sciences*, *67*(4), 963–980. https://doi.org/10.1175/2009JAS3222.1

Kim, Y. J., Eckermann, S. D., & Chun, H. Y. (2003). An overview of the past, present and future of gravity-wave drag parametrization for numerical climate and weather prediction models. *Atmosphere-Ocean*, *41*(1), 65–98. https://doi.org/10.3137/ao.410105

Kleinknecht, N. H., Espy, P. J., & Hibbins, R. E. (2014). The climatology of zonal wave numbers 1 and 2 planetary wave structure in the MLT using a chain of northern hemisphere SuperDARN radars. *Journal of Geophysical Research: Atmospheres*, *119*, 1292–1307. https://doi.org/10.1002/2013JD019850

Kogure, M., Yue, J., Nakamura, T., Hoffmann, L., Vadas, S. L., Tomikawa, Y., et al. (2020). First direct observational evidence for secondary gravity waves generated by mountain waves over the andes. *Geophysical Research Letters*, *47*, e2020GL088845. https://doi.org/10.1029/2020GL088845

Krisch, I., Ern, M., Hoffmann, L., Preusse, P., Strube, C., Ungermann, J., et al. (2020). Superposition of gravity waves with different propagation characteristics observed by airborne and space-borne infrared sounders. *Atmospheric Chemistry and Physics*, *2020*, 1–31. https://doi.org/10.5194/acp-2020-327

Krisch, I., Preusse, P., Ungermann, J., Dörnbrack, A., Eckermann, S. D., Ern, M., et al. (2017). First tomographic observations of gravity waves by the infrared limb imager GLORIA. *Atmospheric Chemistry and Physics*, *17*(24), 14,937–14,953. https://doi.org/10.5194/acp-17-14937-2017

Krisch, I., Ungermann, J., Preusse, P., Kretschmer, E., & Riese, M. (2018). Limited angle tomography of mesoscale gravity waves by the infrared limb-sounder GLORIA. *Atmospheric Measurement Techniques*, *11*(7), 4327–4344. https://doi.org/10.5194/amt-11-4327-2018

Lehmann, C. I., Kim, Y.-H., Preusse, P., Chun, H.-Y., Ern, M., & Kim, S.-Y. (2012). Consistency between Fourier transform and small-volume few-wave decomposition for spectral and spatial variability of gravity waves above a typhoon. *Atmospheric Measurement Techniques*, *5*(7), 1637–1651. https://doi.org/10.5194/amt-5-1637-2012

Liu, X., Xu, J., Yue, J., Vadas, S. L., & Becker, E. (2019). Orographic primary and secondary gravity waves in the middle atmosphere from 16-year SABER observations. *Geophysical Research Letters*, *46*, 4512–4522. https://doi.org/10.1029/2019GL082256

Lomb, N. R. (1976). Least-squares frequency analysis of unequally spaced data. *Astrophysics and Space Science*, *39*(2), 447–462. https://doi.org/10.1007/BF00648343

McLandress, C., Shepherd, T. G., Polavarapu, S., & Beagley, S. R. (2012). Is missing orographic gravity wave drag near 60°S the cause of the stratospheric zonal wind biases in chemistry-climate models? *Journal of the Atmospheric Sciences*, *69*, 802–818. https://doi.org/10.1175/JAS-D-11-0159.1

Meyer, C. I., & Hoffmann, L. (2014). Validation of AIRS high-resolution stratospheric temperature retrievals. *Proceedings of SPIE*, 92420, 9242–9242–10. https://doi.org/10.1117/12.2066967

O'Sullivan, D., & Dunkerton, T. J. (1995). Generation of inertia-gravity waves in a simulated life-cycle of baroclinic instability. *Journal of the Atmospheric Sciences*, *52*(21), 3695–3716. https://doi.org/10.1175/1520-0469

Pawson, S., & Kubitz, T. (1996). Climatology of planetary waves in the northern stratosphere. *Journal of Geophysical Research*, *101*(D12), 16,987–16,996. https://doi.org/10.1029/96JD01226

Plougonven, R., de la Cámara, A., Hertzog, A., & Lott, F. (2020). How does knowledge of atmospheric gravity waves guide their parameterizations? *Quarterly Journal of the Royal Meteorological Society*, *146*(728), 1529–1543. https://doi.org/10.1002/qj.3732

Plougonven, R., & Zhang, F. (2014). Internal gravity waves from atmospheric jets and fronts. *Reviews of Geophysics*, *52*, 33–76. https://doi.org/10.1002/2012RG000419

Polichtchouk, I., & Scott, R. K. (2020). Spontaneous inertia-gravity wave emission from a nonlinear critical layer in the stratosphere. *Quarterly Journal of the Royal Meteorological Society*, *146*(728), 1516–1528. https://doi.org/10.1002/qj.3750

Polichtchouk, I., Shepherd, T. G., Hogan, R. J., & Bechtold, P. (2018). Sensitivity of the Brewer-Dobson circulation and polar vortex variability to parameterized nonorographic gravity wave drag in a High-Resolution atmospheric model. *Journal of the Atmospheric Sciences*, *75*(5), 1525–1543. https://doi.org/10.1175/jas-d-17-0304.1

Preusse, P., Dörnbrack, A., & Eckermann, S. (2002). Space-based measurements of stratospheric mountain waves by CRISTA 1. Sensitivity, analysis method, and a case study. *Journal Geophysical Research*, *107*(D23), 8178. https://doi.org/10.1029/2001JD000699

Preusse, P., Ern, M., Bechtold, P., Eckermann, S. D., Kalisch, S., Trinh, Q. T., & Riese, M.(2014). Characteristics of gravity waves resolved by ECMWF. *Atmospheric Chemistry and Physics*, *14*, 10,483–10,508. https://doi.org/10.5194/acp-14-10483-2014

Rao, J., Garfinkel, C. I., White, I. P., & Schwartz, C. (2020). The southern hemisphere minor sudden stratospheric warming in september 2019 and its predictions in S2S models. *Journal of Geophysical Research: Atmospheres*, *125*, e2020JD032723. https://doi.org/10.1029/2020JD032723

Sato, K., Tateno, S., Watanabe, S., & Kawatani, Y. (2012). Gravity wave characteristics in the Southern Hemisphere revealed by a high-resolution middle-atmosphere general circulation model. *Journal of the Atmospheric Sciences*, *69*, 1378–1396. https://doi.org/10.1175/JAS-D-11-0101.1

Sato, K., Tsuchiya, C., Alexander, M. J., & Hoffmann, L. (2016). Climatology and ENSO-related interannual variability of gravity waves in the southern hemisphere subtropical stratosphere revealed by high-resolution AIRS observations. *Journal Geophysical Research: Atmospheres*, *121*, 7622–7640. https://doi.org/10.1002/2015JD024462

Satomura, T., & Sato, K. (1999). Secondary generation of gravity waves associated with the breaking of mountain waves. *Journal of the Atmospheric Sciences*, *56*(22), 3847–3858. https://doi.org/10.1175/1520-0469(1999)056<3847:SGOGWA>2.0.CO;2

Scargle, J. D. (1982). Studies in astronomical time series analysis. II—Statistical aspects of spectral analysis of unevenly spaced data. *The Astrophysical Journal*, *263*, 835. https://doi.org/10.1086/160554

Smith, A. K., Garcia, R. R., Moss, A. C., & Mitchell, N. J. (2017). The semiannual oscillation of the tropical zonal wind in the middle atmosphere derived from satellite geopotential height retrievals. *Journal of the Atmospheric Sciences*, *74*(8), 2413–2425. https://doi.org/10.1175/jas-d-17-0067.1

Stockwell, R. G., Mansinha, L., & Lowe, R. P. (1996). Localization of the complex spectrum: The S transform. *IEEE Transactions on Signal Processing*, *44*(4), 998–1001. https://doi.org/10.1109/78.492555

Vosper, S. B. (2015). Mountain waves and wakes generated by south Georgia: Implications for drag parametrization. *Quarterly Journal of the Royal Meteorological Society*, *141*(692), 2813–2827. https://doi.org/10.1002/qj.2566

Vosper, S. B., Brown, A. R., & Webster, S. (2016). Orographic drag on islands in the NWP mountain grey zone. *Quarterly Journal of the Royal Meteorological Society*, *142*(701), 3128–3137. https://doi.org/10.1002/qj.2894

Warner, C. D., & McIntyre, M. E. (1996). On the propagation and dissipation of gravity wave spectra through a realistic middle atmosphere. *Journal of the Atmospheric Sciences*, *53*(22), 3213–3235. https://doi.org/10.1175/1520-0469(1996)053<3213:OTPADO>2.0.CO;2

Watanabe, S., Kawatani, Y., Tomikawa, Y., Miyazaki, K., Takahashi, M., & Sato, K. (2008). General aspects of a T213L256 middle atmosphere general circulation model. *Journal Geophysical Research*, *113*, D12110. https://doi.org/10.1029/2008JD010026

Woods, B. K., & Smith, R. B. (2010). Energy flux and wavelet diagnostics of secondary mountain waves. *Journal of the Atmospheric Sciences*, *67*(11), 3721–3738. https://doi.org/10.1175/2009JAS3285.1

Wright, C. J., & Hindley, N. P. (2018). How well do stratospheric reanalyses reproduce high-resolution satellite temperature measurements? *Atmospheric Chemistry and Physics*, *18*(18), 13,703–13,731. https://doi.org/10.5194/acp-18-13703-2018

Wright, C. J., Hindley, N. P., Hoffmann, L., Alexander, M. J., & Mitchell, N. J. (2017). Exploring gravity wave characteristics in 3-D using a novel s-transform technique: AIRS/aqua measurements over the southern andes and drake passage. *Atmospheric Chemistry and Physics*, *17*(13), 8553–8575. https://doi.org/10.5194/acp-17-8553-2017

Wright, C. J., Hindley, N. P., & Mitchell, N. J. (2016). Combining AIRS and MLS observations for three-dimensional gravity wave measurement. *Geophysical Research Letters*, *43*, 884–893. https://doi.org/10.1002/2015GL067233

Wu, D. L. (2004). Mesoscale gravity wave variances from AMSU-A radiances. *Geophysical Research Letters*, *31*, L12114. https://doi.org/10.1029/2004GL019562

Wu, D. L., & Waters, J. W. (1996). Satellite observations of atmospheric variances: A possible indication of gravity waves. *Geophysical Research Letters*, *23*, 3631–3634. https://doi.org/10.1029/96GL02907

Yan, X., Arnold, N., & Remedios, J. (2010). Global observations of gravity waves from High Resolution Dynamics Limb Sounder temperature measurements: A year-long record of temperature amplitude. *Journal Geophysical Research*, *115*, D10113. https://doi.org/10.1029/2008JD011511

Yasui, R., Sato, K., & Miyoshi, Y. (2018). The momentum budget in the stratosphere, mesosphere, and lower thermosphere. Part II: The in situ generation of gravity waves. *Journal of the Atmospheric Sciences*, *75*(10), 3635–3651. https://doi.org/10.1175/JAS-D-17-0337.1